Fast and Robust Symmetry Detection for Brain Images Based on Parallel Scale-Invariant Feature Transform Matching and Voting

Huisi Wu,[1] Defeng Wang,[2] Lin Shi,[2] Zhenkun Wen,[1] Zhong Ming[1]

[1] College of Computer Science and Software Engineering, Shenzhen University, Shenzhen, Guangdong, People's Republic of China

[2] Department of Imaging and Interventional Radiology, The Chinese University of Hong Kong, Shatin, NT, Hongkong SAR, People's Republic of China

Received 10 May 2013; accepted 22 August 2013

ABSTRACT: Symmetry analysis for brain images has been considered as a promising technique for automatically extracting the pathological brain slices in conventional scanning. In this article, we present a fast and robust symmetry detection method for automatically extracting symmetry axis (fissure line) from a brain image. Unlike the existing brain symmetry detection methods which mainly rely on the intensity or edges to determine the symmetry axis, our proposed method is based on a set of scale-invariant feature transform (SIFT) features, where the symmetry axis is determined by parallel matching and voting of distinctive features within the brain image. By clustering and indexing the extracted SIFT features using a GPU KD-tree, we can match multiple pairs of features in parallel based on a novel symmetric similarity metric, which combines the relative scales, orientations, and flipped descriptors to measure the magnitude of symmetry between each pair of features. Finally, the dominant symmetry axis presented in the brain image is determined using a parallel voting algorithm by accumulating the pair-wise symmetry score in a Hough space. Our method was evaluated on both synthetic and in vivo datasets, including both normal and pathological cases. Comparisons with state-of-the-art methods were also conducted to validate the proposed method. Experimental results demonstrated that our method achieves a real-time performance and with a higher accuracy than previous methods, yielding an average polar angle error within 0.69° and an average radius error within 0.71 mm.

© 2013 Wiley Periodicals, Inc.

Int J Imaging Syst Technol, 23, 314–326, 2013; Published online in Wiley Online Library (wileyonlinelibrary.com). DOI: 10.1002/ima.22066

Key words: brain symmetry analysis; SIFT matching; GPU KD-tree; parallel processing

I. INTRODUCTION

It is well-known that human brains have two apparently similar hemispheres, where most tissues in left hemisphere have a mirrored counterpart on the right hemisphere with similar scale and appearance, exhibiting an approximate bilateral symmetry. Researchers also found that such an approximately symmetric structure of human brains would be degenerated with the presence of pathological conditions where abnormal tissue intensity and texture alterations may happen, such as brain tumors (Joshi et al., 2003; Yu et al., 2012), infections (Corti et al., 2008; Hermes et al., 2008), traumatic brain injury (Gilles et al., 2003; Kumar et al., 2005), perinatal brain lesions (Tommasi et al., 2009; Tilman et al., 2010; Roussigne et al., 2012; Saenger et al., 2012), and metabolic disorders (Herbert et al., 2005; Cullen et al., 2006; Takao et al., 2010; Oertel-Knöchel et al., 2011). Recently, symmetry analysis especially systematic and quantitative correlation between asymmetry and specific brain pathologies has been considered as a promising technique to enhance the current computer-aided diagnostic system. Lorenzen et al. (2001) first identified tumors through quantifying structural and radiometric asymmetry. Bergo et al. (2008a, 2008b) also successfully relied on the symmetry location of brain to segment the focal cortical dysplasia in epilepsy. Liu et al. (2007) and Teverovskiy et al. (2008) further discovered the biomarkers in Alzheimer's disease by measuring the brain asymmetry. For effective pathological brain image identification and comparison, most existing state-of-the-art techniques (Brummer, 1991; Ardekani et al., 1997; Liu et al., 2001; Hu et al., 2003; Volkau et al., 2006; Bergo et al., 2008a, 2008b) mainly rely on the identification of the symmetry plane or symmetry axis from the brain images to quantitatively analyze the asymmetry patterns. Without a fast and robust method to automatically extract the symmetry plane or symmetry axis from the brain images, correctly and efficiently evaluating of asymmetry patterns is hard to achieve.

Symmetry plane detection methods (Prima et al., 2002, 2007; Teverovskiy et al., 2006; Song et al., 2007; Zhang et al., 2008) usually assume the global geometry of brain or head to be symmetrical, aiming to identify an optimal mid-sagittal plane (MSP) about which the three-dimensional (3D) anatomical tissues within the given brain image obtain a maximum bilateral symmetry. Existing methods for

---

Correspondence to: Huisi Wu; e-mail: hswu@szu.edu.cn

© 2013 Wiley Periodicals, Inc.

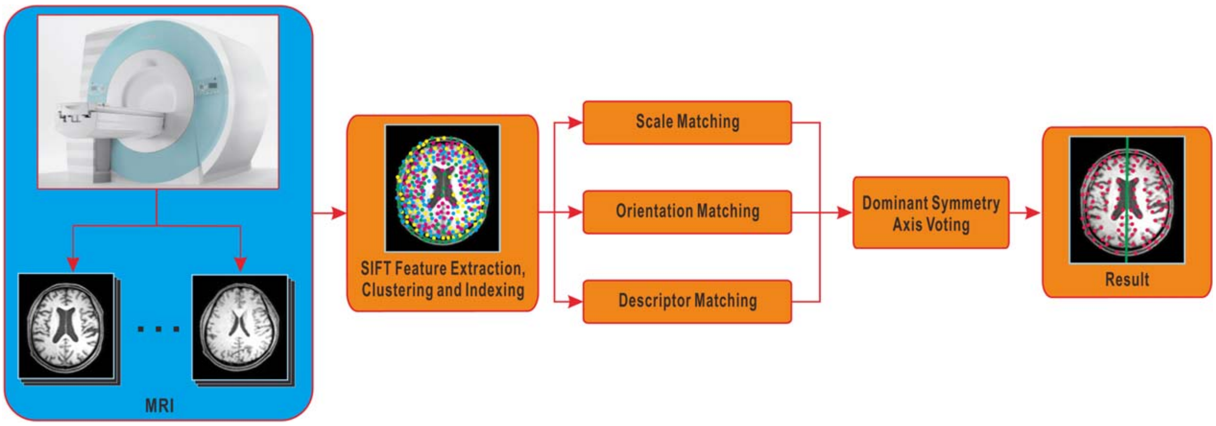

Figure 1. Framework of our method. [Color figure can be viewed in the online issue, which is available at wileyonlinelibrary.com.]

extracting MSP can be broadly divided into two categories (Liu, 2009), namely shape-based and content-based methods. Shape-based methods determine the symmetry plane relying on the detected geometric landmarks or topological features of the head, such as interhemispheric fissure and moments of inertia (Tuzikov et al., 2003; Liu et al., 2011), while content-based methods perform the symmetry plane extraction through registration between the two hemispheres based on internal signal features, such as voxel intensity, local edge, and grayscale distribution (Stegmann et al., 2005; Grigaitis and Meilunas, 2007). However, due to the fact that normal or pathological deformation is commonly seen within human head, there almost never exist perfectly MSP lying on a flat surface, so MSP extracted using both shape-based and content-based methods is ill-defined. Since MSP only provides a coarse symmetry division, only rough asymmetry evaluation can be performed for the global human brain (Roy and Bandyopadhyay, 2012). Instead, symmetry axis detection potentially enables us to perform a tailor-made asymmetry evaluation for brain images by accurately extracting the regional symmetry line and retrieving the pathological slices. On the other hand, symmetry plane detection is generally much more computational intensive than symmetry axis detection.

Symmetry axis detection methods focus on estimating the 2D mid-sagittal axis for each coronal or axial slice, which has also been intensively studied (Gong et al., 2005; Costantini et al., 2007; Liu et al., 2008). Several MSP extraction methods are based on detecting the symmetry axes slice by slice. Junck et al. (1990) first used cross-correlation analysis to detect the symmetry axis within a transverse positron emission tomography (PET) or single-photon emission computed tomography (SPECT) slice. Brummer (1991) used a Hough transformation to compute the longitudinal fissure at each coronal slice. Liu et al. (2001) presented an edge-based, cross-correlation approach to discover symmetry axis on each coronal or axial slice. Hu et al. (2003) relied on an exhaustive search algorithm to determine the optimal parameters of the symmetry axis. More recently, Song et al. (2007) defined a moment of gravitational force and identified the symmetry axis based on the correlation of gray level distribution. Costantini and Casali (2007) proposed a cellular neural network based algorithm for symmetry axis detection. Liu et al. (2008) formulated the symmetry detection as an optimization problem and used an interactive searching algorithm to solve the optimal symmetry axis. Ruppert et al. (2011) applied a correlation of detected edges to extract the symmetry axis. Although promising improvements have been made in both methodology and performance, the existing methods for symmetry axis detection from brain images are still not reliable enough and too time consuming to be used in clinical applications. In addition, they mainly used gray level, skull shape or edges to infer the symmetry axis, which may easily suffer from difficulties caused by image noise, local deformation, or the deficiencies of edge detectors. Also, the computation procedure using iterative optimization scheme cannot achieve real-time performance.

In this study, we present a fast and robust symmetry axis detection method based on parallel SIFT matching and voting. Figure 1 overviews our framework, unlike the previous methods, we first apply the well-known SIFT algorithm to capture a set of features, which is implemented with graphics processing units (GPU). Since SIFT descriptor is invariant to scaling, orientation, affine distortion, and intensity changes, correlation on SIFT features prevents suffering from the image noise, local deformation, and the deficiencies of edge detectors. In addition, a GPU KD-tree is also built to index the clustered SIFT features, which allows parallel matching and voting multiple pairs of features to determine the fissure line. For effectively measuring the magnitude of symmetry between two SIFT features, a novel symmetric similarity metric is defined by considering their relative scales, orientations, and flipped descriptors. Based on the parallel SIFT matching and voting, the dominant symmetry axis presented in the brain image is finally determined by accumulating the pairwise symmetry score in a Hough space. Our method was evaluated

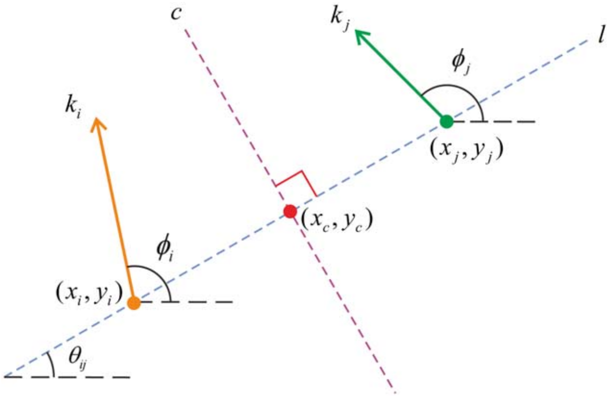

Figure 2. Symmetric orientations of a pair of features. [Color figure can be viewed in the online issue, which is available at wileyonlinelibrary.com.]

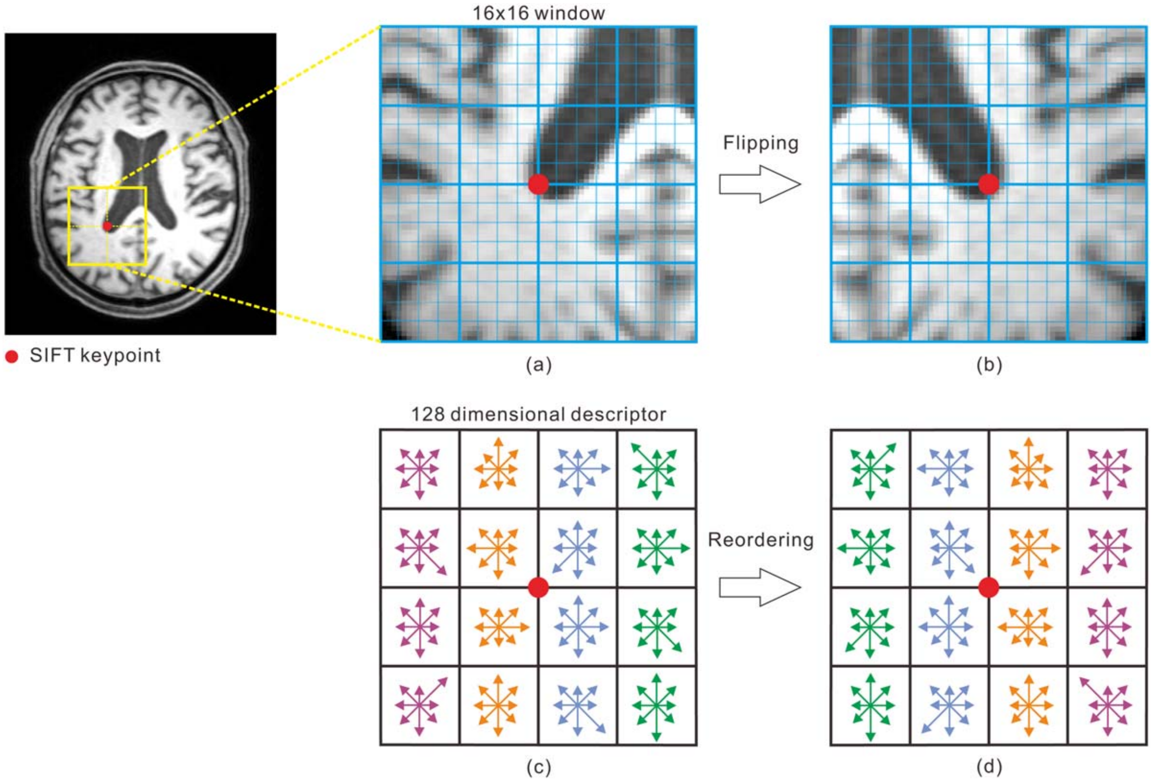

Figure 3. Formation of a mirrored SIFT descriptor for a flipped image patch. For a flipped image patch (b), the mirrored SIFT descriptor in (d) is obtained by reordering the original SIFT descriptor in (c). [Color figure can be viewed in the online issue, which is available at wileyonlinelibrary.com.]

on both synthetic mirrored images and in vivo datasets, including both normal and pathological cases. Convincing experiment results and comparisons demonstrated the effectiveness of our method.

II. METHODOLOGY

A. Feature Detection.

To achieve efficient and robust symmetry detection for brain images, we propose a novel framework by matching symmetric pairs of distinctive feature points within the brain images. Although existing feature detection and feature matching methods have been widely used for generating dense correspondences between images, there were rare reports of searching inner correspondences by matching pairs of feature points within a single image. Since the approximate symmetry structure of human brain implies that there exist a set of mirrored features within the brain images, we can explore this to develop a fast and robust algorithm for symmetry detection in the brain images.

Given a brain image, we first detect a set of feature points using SIFT algorithm (Lowe, 2004), as shown in Figure 1. By applying difference of Gaussians functions to obtain a series of smoothed and resampled images, we can identify a set of key locations via extracting maxima and minima in scale space. We also discard low contrast candidate points and edge response points along an edge and assign dominant orientations to localized keypoints, such that the keypoints are more stable for matching and recognition. We denote each keypoint as a four-dimensional vector $k_i = (x_i, y_i, s_i, \phi_i)$, where (x_i, y_i), s_i, and ϕ_i describe its location, scale, and orientation, respectively. Such a four-dimensional vector typically defines each feature's location, scale, and orientation for fast matching. To determine the symmetric relationship of pairs of feature points, we still have to measure the local appearance of each feature point. Hence, a SIFT feature descriptor $p_i = (v_1, v_2, \ldots v_{128})$ is generated for each keypoint k_i to encode the local appearance of the feature point after its scale and orientation have been normalized. Similar with Lowe (2004), we generate each SIFT descriptor based on a 16×16 gradient kernel, which is rotated with respect to the keypoint orientation ϕ_i and divided into 4×4 subregions. Each subregion is characterized by the gradient contributions to an eight-bin orientation histogram. Concatenation of the 16 orientation histograms creates SIFT's 128-element (16 subregions $\times$ 8 orientation bins) descriptor vector $p_i = (v_1, v_2, \ldots v_{128})$. The distinctiveness of k_i, together with the scale-invariant and rotation-invariant p_i, provide a fast and robust mean which is particularly well-suited to detecting pairs of symmetric features.

B. Clustering and Indexing.

The reflectional symmetry structure in human brain normally contains multiple pairs of symmetric elements. Normally, the number of SIFT features is about 600–800 when the resolution of the brain magnetic resonance (MR) image is 256×256, and the number will exceed 1000 for a resolution of 512×512. Under such scenario, we cannot use a simple geometric heuristics to effectively cull the potential matches. Even for using best-bin first matching algorithm (Lowe, 2004), it still costs about 0.8 s to pick out all potential matches, which is still too time consuming to achieve a real-time performance, because a brain examination normally contains about 200–300 slices. As similar elements should have similar SIFT features, this suggests that we can perform clustering on the SIFT keypoints to accelerate the feature matching. We use adaptive mean-shift clustering (Comaniciu and Meer, 2002) to group

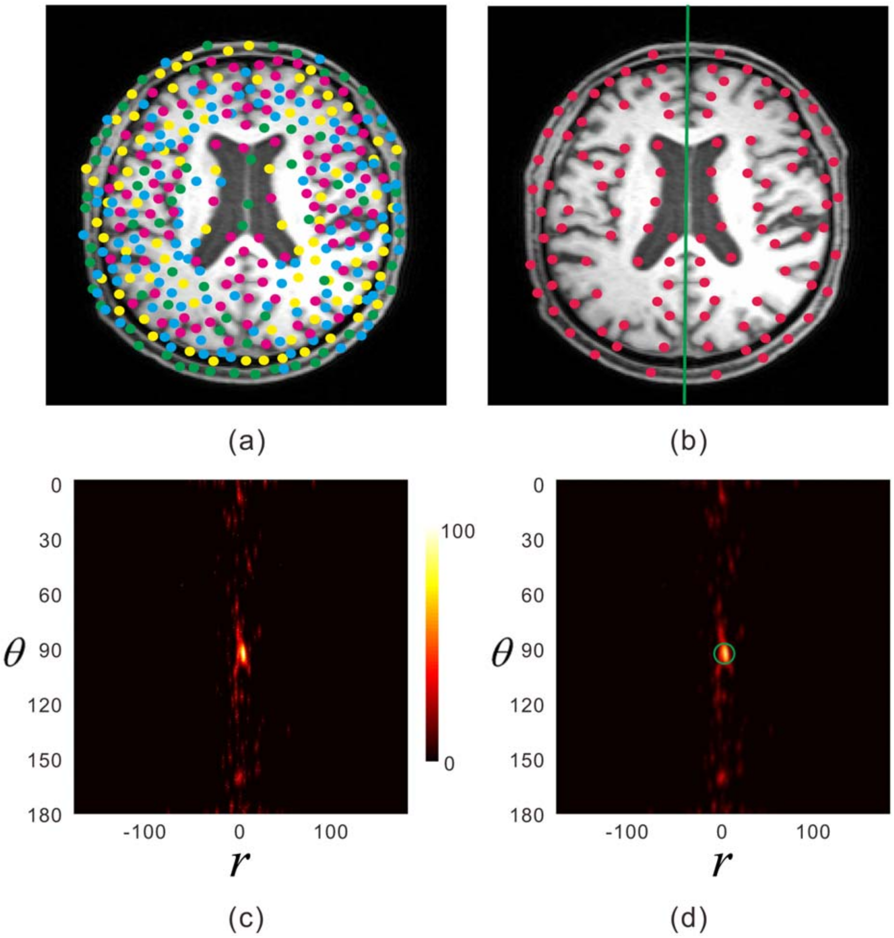

Figure 4. Voting the dominant symmetry axis. (a) Clustered SIFT keypoints in a brain MR image (256 × 256). (b) Dominant symmetry axis voted and the symmetric features associated with it. (c) Symmetry axes in Hough space. (d) Extraction of the center of the convex hull in the Hough space (applied a strand Gaussian filter). [Color figure can be viewed in the online issue, which is available at wileyonlinelibrary.com.]

the detected SIFT feature points. Similar with Zhou et al. (2010), our mean-shift clustering algorithm is also implemented on GPU by using compute unified device architecture (CUDA). The major advantage of parallel mean-shift clustering is it can automatically determine the number of clusters, which otherwise requires knowing the number of clusters in advance by using other techniques, such as *k*-means. In our implementation, the scales s_i of all detected keypoints are fed for adaptive mean-shift clustering to group features with similar shapes and sizes.

To enable parallel matching and voting multiple pairs of features, we also use a GPU KD-tree to index the clustered SIFT features. Specifically, to facilitate the following *k*-nearest neighbor (KNN) searching in symmetry matching, we further index the scales s_i of keypoints in each cluster with a KD-tree (Zhou et al., 2008). For fast retrieval, we implemented the KD-tree on GPU to support the parallel KNN searching.

C. Symmetric Similarity Metric. We can then form symmetric pairs of feature points for each cluster by matching a keypoint with its nearest neighbors. However, the resulting pairs of features may potentially contain different things, as the clustering is only based on a crude measurement of shape and size without considering the region content. Hence, we need a more sophisticated metric to validate and select neighbors during making a symmetric pair of feature points. We define a metric to quantify the symmetric similarity of two neighboring SIFT keypoints in terms of scale, orientation, and appearance.

C.1. Scale Similarity. Even when the symmetry structure is slightly deformed, two symmetric elements remain close in shape and size. Hence, the shape similarity S_{ij} of two symmetric features k_i and k_j is a function of their scale

$$S_{ij}=\exp\left(\frac{-\|s_i-s_j\|^2}{\sigma_s}\right) \tag{1}$$

where σ_s controls the weighting of the scale variation, $\sigma_s = 1$ was used in our experiments.

C.2. Orientation Symmetric Similarity. For each pair of symmetric keypoints k_i and k_j, their orientations should also exhibit mirror symmetry. Hence, we design a orientation symmetric similarity Φ_{ij} to measure the angular similarity in terms of their orientation. As shown in Figure 2, suppose the line passing through k_i and k_j is denoted as l. According to the phase weighting method presented in Reisfeld et al. (1995), we denote the orientation symmetric similarity Φ_{ij} as

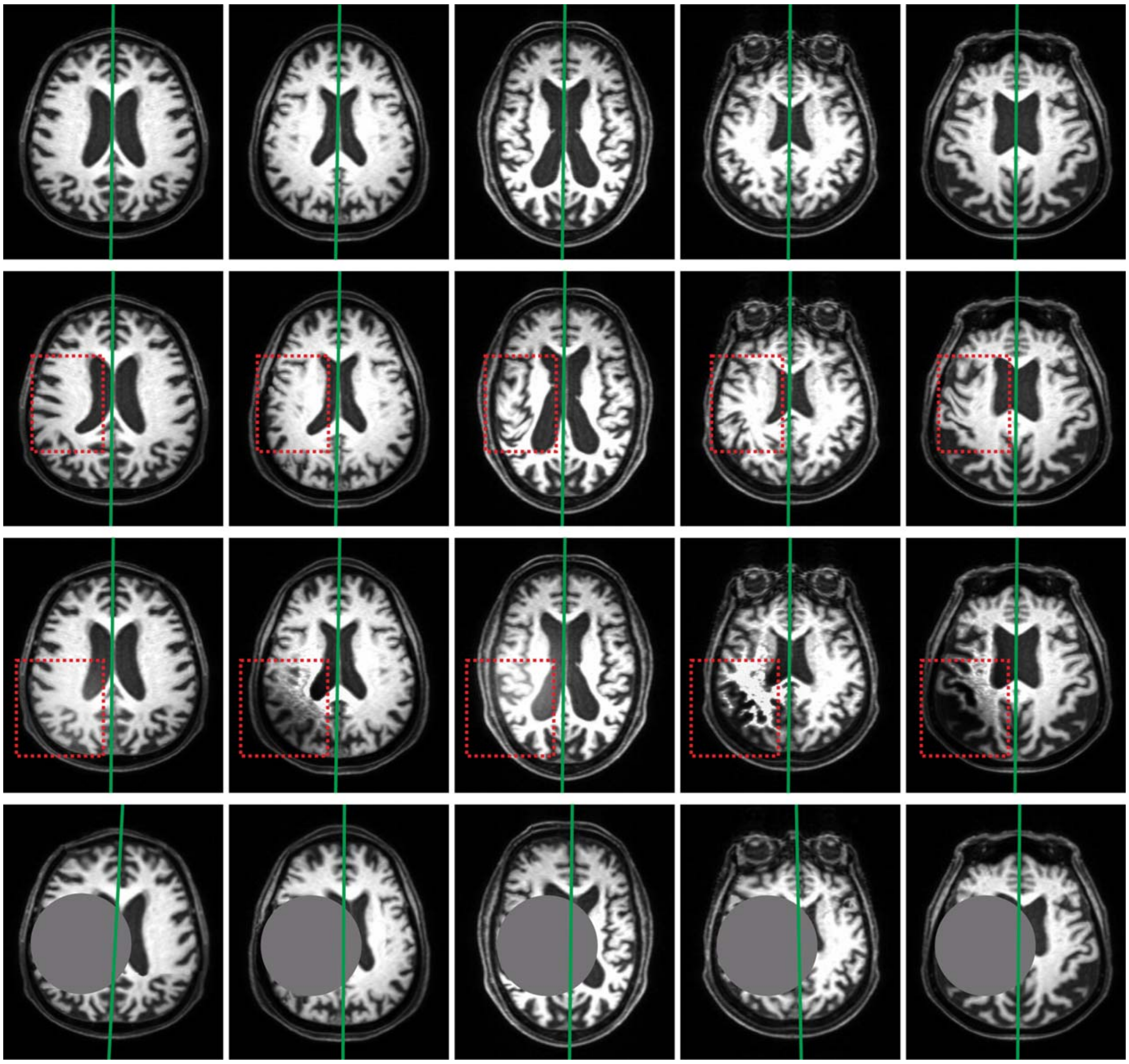

Figure 5. Symmetry axes extracted from synthetic images with known ground truth (first row). Local distortion, bias inhomogeneity, and artificial tumor are added to the original image (shown in second, third, and fourth rows, respectively). [Color figure can be viewed in the online issue, which is available at wileyonlinelibrary.com.]

$$\Phi_{ij}=\frac{1-\cos\left(\phi_i+\phi_j-2\theta_{ij}\right)}{2} \tag{2}$$

where ϕ_i, ϕ_j, and θ_{ij} are the angles counterclockwise between the horizontal line and k_i, k_j, or l, respectively. We can easily observe that $\Phi_{ij}\in[0,1]$, with larger value when the orientations of k_i and k_j are more symmetric similar with each other.

C.3. Appearance Symmetric Similarity. Since scale similarity and orientation symmetric similarity between keypoints k_i and k_j do not consider the image appearance, we further measure their appearance symmetric similarity by comparing their descriptors p_i and p_j, which encode the local image patches associated with k_i and k_j, as shown in Figure 3c. The detailed mathematical definition of SIFT descriptor and its implementation can be found in Lowe (2004). Although SIFT descriptor is scale-independent and orientation-independent after scale and orientation normalization, we still cannot define the appearance symmetric similarity by directly calculating the distance between p_i and p_j. That is because SIFT descriptor is not flipping-invariant. Similar with Zhao and Ngo (2013), we first form a mirrored SIFT descriptor q_i by recording the 128 elements within p_i, as shown in Figure 3. Then, we denote the appearance symmetric similarity Ω_{ij} as

$$\Omega_{ij}=\exp\left(\frac{-\|q_i-p_j\|^2}{\sigma_a}\right) \tag{3}$$

where σ_a controls the weighting of the appearance variation, $\sigma_a=0.5$ was used in our experiments.

All the above-defined scale, orientation, and appearance weightings are combined to form an overall symmetric similarity metric M_{ij} for each pair of keypoints k_i and k_j

$$M_{ij}=S_{ij}\times\Phi_{ij}\times\Omega_{ij} \tag{4}$$

So far, we can use $M_{ij}\in[0,1]$ to quantify the symmetry magnitude for an individual pair of keypoint vectors. Since the symmetry structure in a brain MR image usually contains a set of symmetric

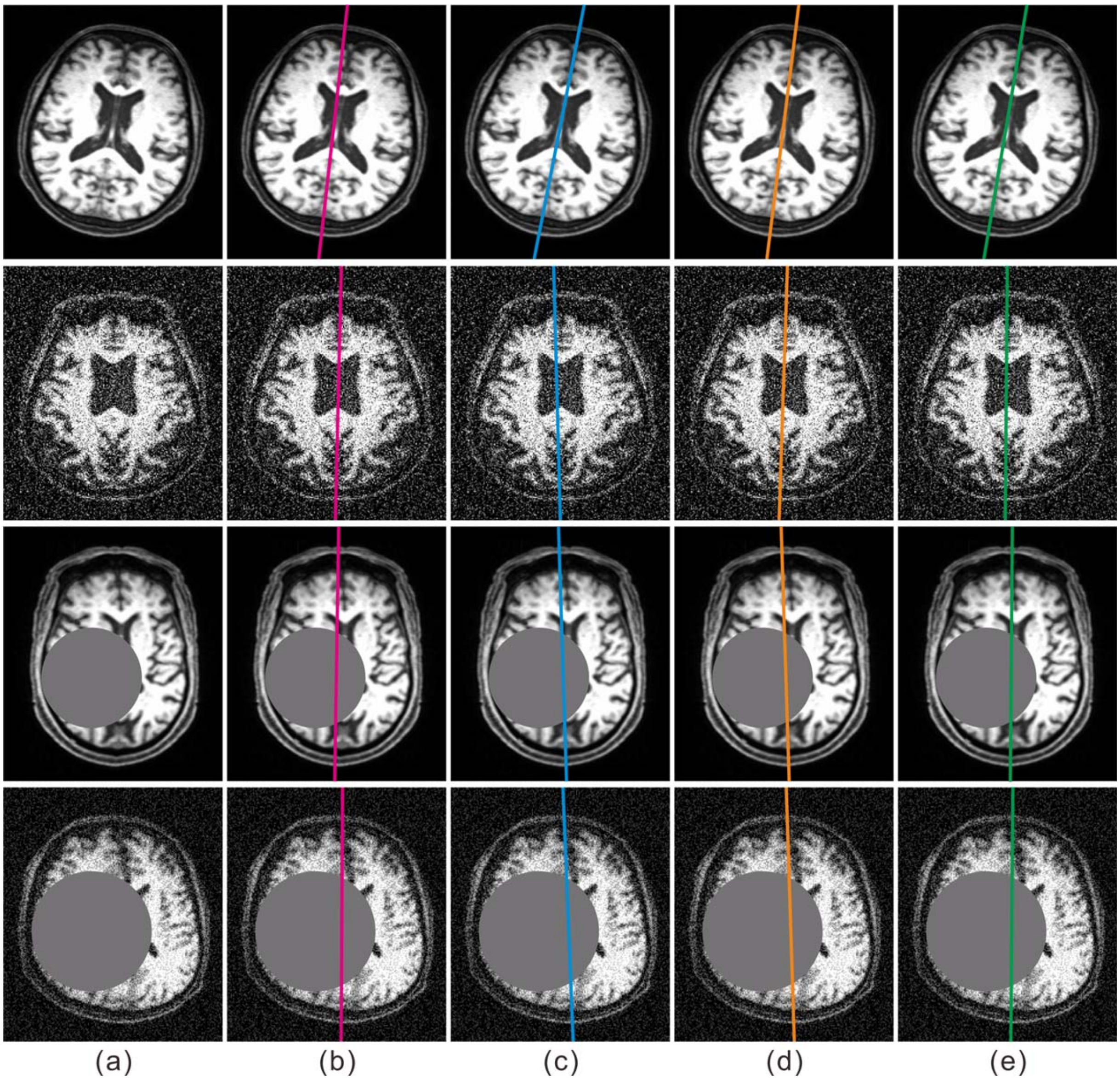

Figure 6. Visual comparison of different methods in detecting symmetry axes from synthetic datasets. (a) Synthetic images. Symmetry axes extracted from (a) using Hu et al. (2003), Song et al. (2007), Ruppert et al. (2011), and our method are shown in (b), (c), (d), and (e), respectively. [Color figure can be viewed in the online issue, which is available at wileyonlinelibrary.com.]

keypoints, we need to accumulate the symmetry magnitudes exhibited by all individual pairs in a voting space to determine the dominant symmetry present in the brain MR image.

D. Dominant Symmetric Axis Voting. To determine the dominant symmetry axis within a brain MR image, we use the standard polar coordinate (r, θ) to represent the potential symmetry axis line c passing perpendicularly through the mid-point of the line joining k_i and k_j, as shown in Figure 2. Under the standard polar coordinate, we denote the potential symmetry axis line c as

$$r_{ij}=x_{\mathrm{c}}\cos\theta_{ij}+y_{\mathrm{c}}\sin\theta_{ij} \tag{5}$$

where (x_{c}, y_{c}) is the centred coordinates of the mid-point of line joining k_i and k_j, and θ_{ij} is the angle counterclockwise between the horizontal line and l.

We then use the linear Hough transform to vote the dominant symmetry axis within the brain MR image. Recall that we have built GPU KD-trees for all detected SIFT keypoints in Section II.B. Hence, we can form a number of pairs of feature points by matching each keypoint with its k-nearest neighbors. Each pair of feature points cast a vote (r_{ij}, θ_{ij}) in Hough space weighted by their symmetry magnitude M_{ij}. Since the voting processes for all pairs of keypoints are independent with each other, we implement the above voting process in a multithreaded GPU using CUDA. So the above voting is done simultaneously in parallel for all selected pairs.

Finally, the dominant symmetry axis within the brain MR image is obtained by extracting the maxima of the final voted Hough space. To avoid the noise in extracting the maxima, we also apply a strand Gaussian filter to blur the final voting result. The maxima is then extracted by identifying the center of the convex hull in the Hough

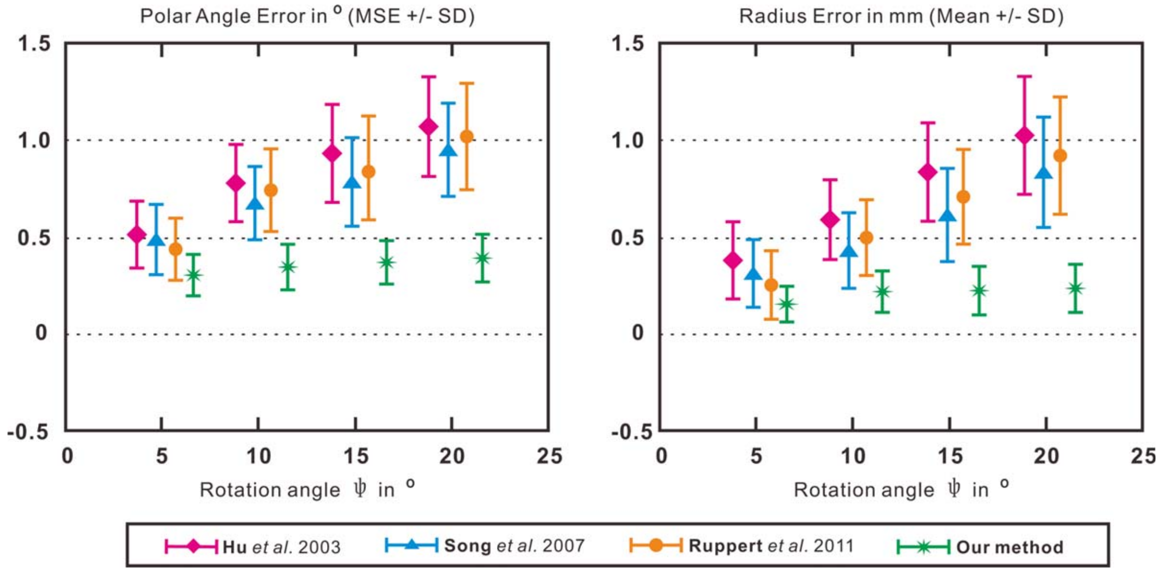

Figure 7. Comparison of different methods in tolerance to rotation. [Color figure can be viewed in the online issue, which is available at wileyonlinelibrary.com.]

space. All neighboring points of the maxima in Hough space are associated with the same dominant symmetry axis within the brain MR image. Figure 4 shows the detailed steps involved in voting the dominant symmetry axis.

III. RESULTS

We implemented our method in C language on a PC with 4 Intel(R) Xeon(TM) CPUs 3.20 GHz, 16 GB RAM, and nVidia GeForce GTX 690 GPU with 4 GB video memory. To evaluate the effectiveness of our proposed method, we test it on both synthetic and in vivo MRI datasets.

A. Evaluation on Synthetic Datasets. Since no human brain exhibits perfect reflectional symmetry, it is difficult to manually identify a symmetry axis to be the ground truth that can be directly used for evaluation. To avoid the subjective factors in visual inspection, we chose to synthesize artificially symmetric images with known ground truth for quantitative testing. Each synthetic image is constructed as following two steps. First, we manually extract a symmetry axis by identifying the fissure line. Then, we reflect one half of the brain image about its symmetry axis to form the other mirrored half. So we can synthesize a perfectly symmetrical image where the ground truth is known.

Given the synthetic datasets, we applied our method to detect the symmetry axis from each brain image. Figure 5 shows the representative resulting slices (with a resolution of 256 × 256). From the upper row, we can see that our method can accurately identify the symmetry axes presented in the brain images. To evaluate the ability of preventing the interference from local distortion, MRI bias

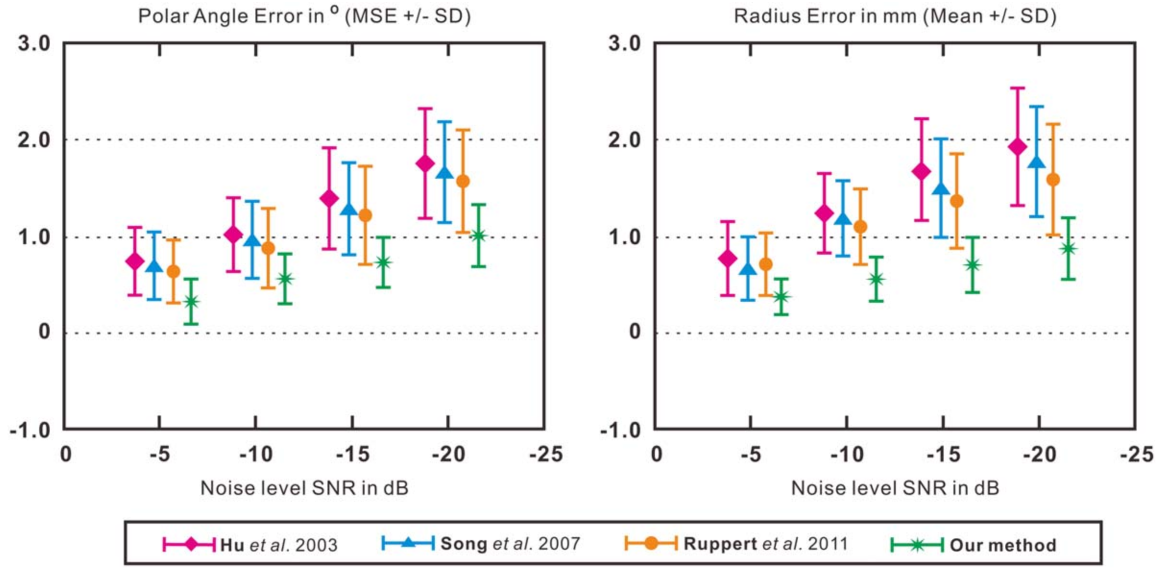

Figure 8. Comparison of different methods in tolerance to noise. [Color figure can be viewed in the online issue, which is available at wileyonlinelibrary.com.]

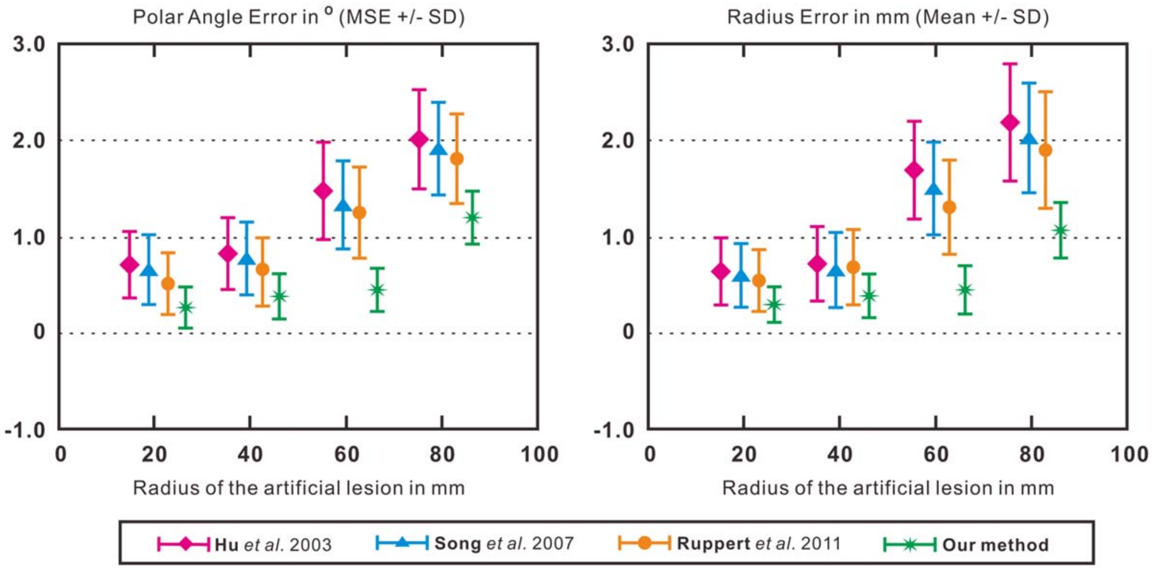

Figure 9. Comparison of different methods in tolerance to asymmetry. [Color figure can be viewed in the online issue, which is available at wileyonlinelibrary.com.]

inhomogeneity or asymmetry structures, we also manually added locally distorted regions, bias inhomogeneities and artificial tumors to the synthetic images, and applied our method to detect the symmetry axes. As shown in the bottom three rows of Figure 5, the impacts of both local distortion and MRI bias inhomogeneities are minimal. Also, we can see that our method can successfully identify the fissure lines, even when the artificial tumors covers about one third of the human brain. But our method can no longer preserve the accuracy of the symmetry axis extraction if the distorted, MRI bias or tumor area is larger than 40% of the human brain. In our experiments, we produced an artificial tumor by drawing a circle in the lower left quarter with a uniform gray level. We also added a local and known nonrigid deformation to the brain near the simulated tumors, as shown in Figures 5 and 6.

To compare our method with state-of-the-art methods, we also implemented three representative methods, including Hu et al. (2003), Song et al. (2007), and Ruppert et al. (2011). For quantitative validation of our method in tolerance to rotation, noise, and asymmetry, we applied our method and the other three competitors to three synthetic datasets with different rotation angles, different noise levels, and different asymmetry ratio, respectively. Symmetry axes detected using Hu et al. (2003), Song et al. (2007), Ruppert et al. (2011), and our method are shown in Figures 6b, 6c, 6d, and 6e, respectively. Since Hu et al. (2003) relied on the pixel by pixel (or line by line) gray level similarity and used an exhaustive search algorithm to detect the symmetry axis, it cannot achieve a high accuracy, especially when suffered from rotation or there have deformation, noise, or asymmetry contents (Fig. 6b). Song's method used the skull contour to determine the symmetry axis and obtained a result better than Hu's method as shown in Figure 6c. On the other hand, by detecting the principle edges using a Sobel operator and fitting the symmetry axis based on edge matching, Ruppert et al. (2011) obtained comparable results versus Song's method, as shown in Figure 6d. But without using a high distinctive image feature to identify the symmetry axis, all of above methods are sensitive to image rotation, noise, and asymmetry. Instead, by using the well-validated SIFT feature to detect symmetry axis, our method outperforms the three competitors in terms of accuracy of symmetry detection. Since SIFT has been proved to be invariant to scaling, orientation, affine distortion, and intensity changes, our method is more stable in preventing the interference from noise, blur, or asymmetry and obtains better results than the other three state-of-the-art methods, as shown in Figure 6e. The bottom row of Figure 6 shows a worst case of our method in symmetry detection, where the simulated tumor area is about 40% of the human brain and the noise level SNR is −25 dB.

Table I. Accuracy statistics of different methods over all simulated datasets. 44×14mm (300 × 300 DPI)

	Polar Angle Error (°)			Radius Error (mm)		
Method	Mean	SD	*P*-value	Mean	SD	*P*-value
Hu et al. 2003	1.253	0.424	0.0052	1.305	0.392	0.0041
Song et al. 2007	1.176	0.389	0.0087	1.206	0.364	0.0096
Ruppert et al. 2011	0.912	0.297	0.0130	1.031	0.317	0.0128
Our method	0.610	0.257		0.709	0.283	

Each P-value is obtained using mixed model analysis to compare our method with the indicated state-of-the-art method.

Besides visual comparison, we also calculated the polar angle error (in degrees) and radius error (in mm) between detected symmetry axis (r_d, θ_d) and the ground truth symmetry axis (r_g, θ_g) to quantitatively compare our method with the other methods. Figures 7, 8, and 9 plot the mean squared error and standard deviation between (r_d, θ_d) and (r_g, θ_g) for our method and the other three competitors over the synthetic datasets with rotation, noise, and asymmetry, respectively. In Figure 9, we used artificial tumor lower left quarter. From the comparison, we can see that our method generally outperforms the other three methods in term of both polar angle accuracy and radius accuracy, with more significant improvement when there is larger rotation angle (Fig. 7), heavier noise (Fig. 8), or larger asymmetry ratio (Fig. 9). This points out the important of using a more distinctive image feature to detect symmetry axis.

Table I shows the statistics of polar angle error and radius over all three synthetic datasets. From the statistics results, we can clearly observe that our method can not only improve the accuracy of polar angle fitting but also the radius of the detected symmetry axis. To

Table II. Breakdown time statistics for Hu et al. 2003, Song et al. 2007, Ruppert et al. 2011, and our method with and without GPU implementation (in seconds). 219×274mm (300 × 300 DPI)

Method	**Hu** et al. 2003				
Image size	Initialization	Searching	Refine	Others	Total
128×128	0.821	2.383	2.216	0.001	5.421
256×256	1.023	3.822	3.698	0.001	8.544
512×512	1.313	6.995	5.323	0.001	13.632

Method	**Song** et al. 2007				
Image size	Contour	RMGF	Iteration	Others	Total
128×128	0.748	0.836	0.965	0.001	6.962
256×256	1.072	1.235	1.833	0.001	4.141
512×512	1.381	2.353	3.227	0.001	6.962

Method	**Ruppert** et al. 2011				
Image size	Edge	Correlation	Iteration	Others	Total
128×128	0.688	1.493	1.252	0.001	3.434
256×256	0.796	2.632	2.517	0.001	5.946
512×512	0.931	3.752	3.193	0.001	7.877

	Our method(without GPU)					
Method Image size	SIFT	Clustering	Indexing	Matching & Voting	Others	Total
128×128	0.586	0.324	0.251	0.367	0.001	1.529
256×256	0.793	0.622	0.423	0.556	0.001	2.395
512×512	0.975	0.936	0.628	0.749	0.001	3.289

	Our method(with GPU)					
Method Image size	SIFT	Clustering	Indexing	Matching & Voting	Others	Total
128×128	0.014	3.75×10^{-6}	2.81×10^{-8}	1.87×10^{-3}	1.17×10^{-6}	0.016
256×256	0022	3.75×10^{-6}	2.81×10^{-8}	2.03×10^{-3}	1.17×10^{-6}	0.024
512×512	0.036	3.75×10^{-6}	2.82×10^{-8}	2.18×10^{-3}	1.18×10^{-6}	0.038

evaluate if our improvement is statistically significant, we also calculated a *P*-value using mixed model analysis to compare our method with each state-of-the-art method. As shown in Table I, compared with other methods, our method has significant improvement in terms of accuracy of both polar angle and radius at the 5% level (*P*-value is less than 0.05). To compare the speed of our method with other three state-of-the-art methods, we further collected the time statistics of different methods over the simulated datasets. To evaluate the impact of the image resolution, we resized each synthesized image from 256 × 256 to 128 × 128/512 × 512 by downsampling/upsampling. For a fair comparison, we implemented our method with and without GPU and compared our method with all competitors on the same PC with 4 Intel(R) Xeon(TM) CPUs 3.20 GHz, 16 GB RAM. As shown in Table II, we collected the breakdown time statistics for each method to perform a clear comparison. Note that, the breakdown time statistics tables are conducted via calculating the average running time on each step for a single MRI image. For all four competitors, the total computation time of each method on the indicated resolution is shown in column "Total," and the "Others" refers to the time for memory adjustment as well as data transfer. Specifically, Hu et al. (2003) relied on the intensity similarity to cull symmetric pixels and used an exhaustive search algorithm to detect the symmetry axis. The "Initialization" refers to coarse determination of the searching region, while "Coarse searching" and "Refine" refer to locating the fissure line using coarse and fine searching, respectively. Song's method employed the skull contour to determine the symmetry axis. The "Contour" in Table II refers to the contour detection for skull, while "resultant moment gravitational force (RMGF)" and "Iteration" indicate the estimation of initial moment gravitational force and the optimization time respectively. Ruppert et al. (2011) fits the symmetry axis based on matching principle edges. The "Edge" and "Correlation" in Table II refer to edge detection using an optimized Sobel operator and the symmetric principle edges' correlation. From the results shown in Table II, we can observe that our method outperforms the other three methods by detecting the symmetry axes with much less running time. Without GPU implementation, our method is about two times faster than the competitors. While relying on the GPU implementation from SIFT detection to parallel matching and voting, our method turns out to be two orders of magnitude faster than the previous methods. Note that, the time of "Clustering" and "Indexing" in our methods are very tiny because the number of SIFT feature points is small (e.g., only about 1300 SIFT features for 512 × 512 images), which is still indicating that the steps of clustering and indexing are important and helpful in exchanging efficiency in turn only with tiny time cost. As shown in Table II, even when the image resolution is 512 × 512, our method still achieves a real time performance.

B. Evaluation on In Vivo Datasets. On the other hand, we also evaluated our proposed method on the in vivo datasets. We collected brain MR images on both normal human and patients, including FLAIR, T_1-weighted and T_2-weighted MRI. As shown in Table III, a total of 646 clinical images were collected, including 136 slices from normal subjects and 510 slices from patients with stroke, infarct, Alzheimer, or tumor. Given the in vivo datasets, we applied our method and the other three state-of-the-art methods to detect the symmetry axes. Selected representative slices detected using Hu et al. (2003), Song et al. (2007), Ruppert et al. (2011) and our method are shown in Figures 10c, 10d, 10e, and 10f, respectively. Since there has no ground truths for the in vivo datasets, we invited a human expert to manually mark the symmetry axes to compare all methods with the human performance. Figure 10b show the slices marked by the expert. From the visual comparison on the Figure 10, we can see that none of Hu et al. (2003), Song et al. (2007), and Ruppert et al. (2011) can achieve a stable symmetry detection because they rely on the gray level, skull shape, or internal edges to determine the symmetry axes, which is sensitive to local image deformation, noise, or asymmetry. Instead, by using a more stable and distinctive SIFT

Table III. In-vivo datasets collected for evaluation. 53×29mm (300 × 300 DPI)

Dataset	Pathology	# of Slices
1	Stroke	129
2	Infarct	127
3	Alzheimer	123
4	Tumor	131
5	Normal	136

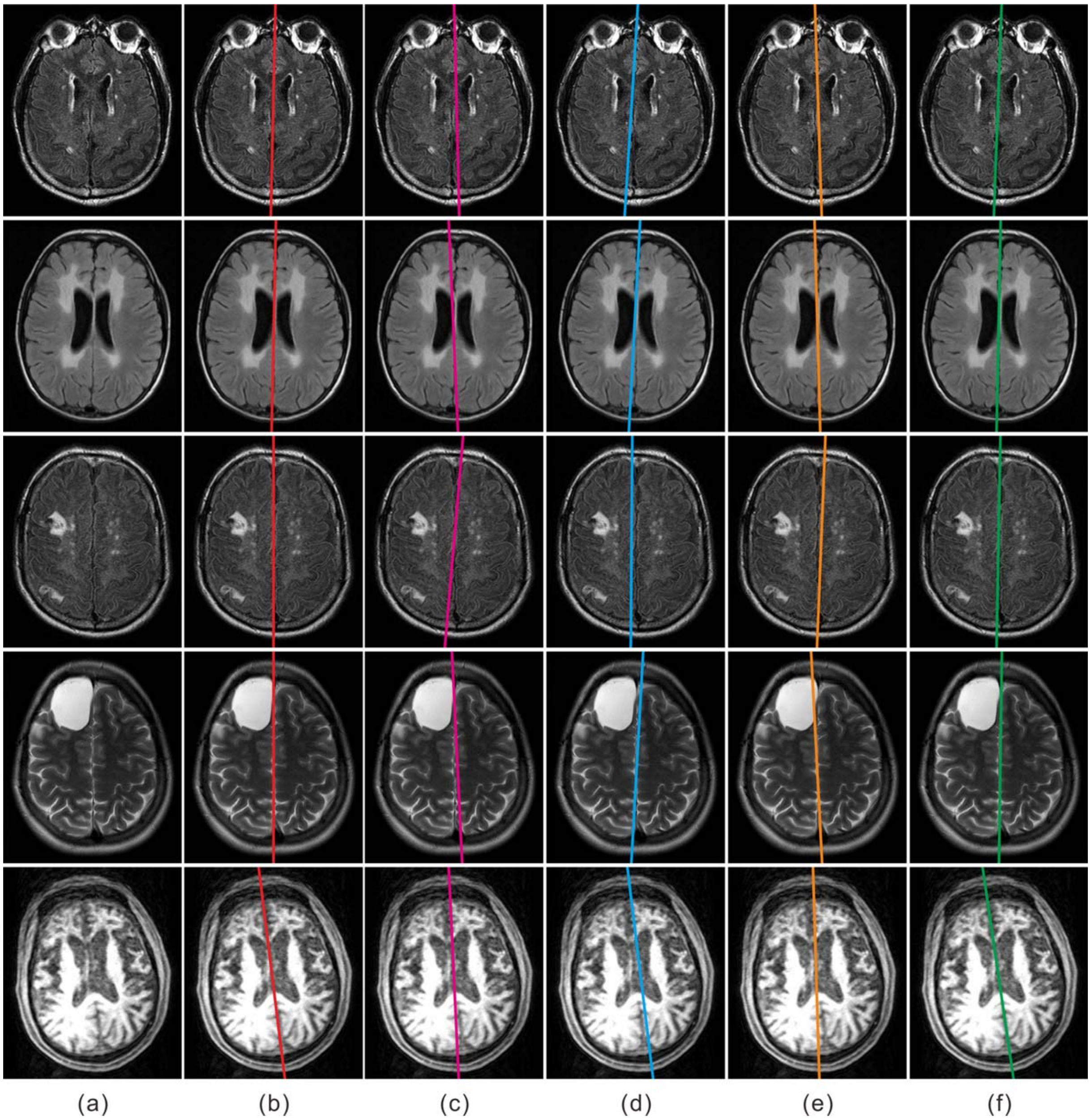

Figure 10. Comparison of different methods in detecting symmetry axes from in vivo datasets. The top three cases are FLAIR MRI. The fourth and the bottom cases are T_2-weighted and T_1-weighted MRI, respectively. (a) Original images. (b) Symmetry axes drawn manually by a human expert. Symmetry axes detected using Hu et al. (2003), Song et al. (2007), Ruppert et al. (2011), and our method are shown in (c), (d), (e), and (f), respectively. [Color figure can be viewed in the online issue, which is available at wileyonlinelibrary.com.]

feature to determine the symmetry axes, our method generally outperforms the other methods, especially on the pathological slices that usually present accentuated asymmetry due to the presence of tumors or variation of the brain tissues. In the experiments for real cases, we applied our method to different types of MR images without any parameter adaption, including FLAIR, T_1-weighted and T_2-weighted, as shown in Figure 10f. Our results are more close to the human expert's results in Figure 10b, when compared to other three methods in Figure 10c, 10d, and 10e, respectively.

Besides visual comparison, we further calculated the polar angle error (in degrees) and radius error (in mm) between detected the symmetry axis (r_d, θ_d) and the human expert's result (r_h, θ_h) to quantitatively compare our method with the other methods. Table IV shows the statistics of accuracy for different methods over each dataset in Table III. From the statistics comparison in Table IV, we can see that our method generally outperforms the other three competitors in term of both polar angle accuracy and radius accuracy, indicating that using a more distinctive SIFT feature to perform symmetry detection is effective. To evaluate if our improvement is statistically significant, we also calculated a P-value using mixed model analysis to compare our method with each state-of-the-art method. As shown in Table IV, compared with other methods, our method has significant improvement in terms of accuracy of both polar angle and radius at the 5% level (P-value is less than 0.05).

We further compared the running time of our method with the other three methods. The statistics of running time for different

Table IV. Accuracy statistics of different methods for each in-vivo dataset. 106×54mm (300 × 300 DPI)

	Polar Angle Error (°)										
	Hu et al. 2003			**Song** et al. 2007			**Ruppert** et al. 2011			**Our method**	
Dataset	Mean	SD	*P*-value	Mean	SD	*P*-value	Mean	SD	*P*-value	Mean	SD
1	1.512	0.431	0.0056	1.354	0.338	0.0087	1.192	0.293	0.0126	0.725	0.263
2	1.483	0.425	0.0049	1.338	0.341	0.0084	1.186	0.287	0.0122	0.702	0.258
3	1.505	0.430	0.0048	1.365	0.353	0.0079	1.203	0.299	0.0128	0.731	0.270
4	1.496	0.428	0.0053	1.351	0.330	0.0083	1.175	0.283	0.0125	0.698	0.256
5	1.488	0.423	0.0055	1.329	0.322	0.0086	1.141	0.275	0.0131	0.686	0.251

	Radius Error (mm)										
	Hu et al. 2003			**Song** et al. 2007			**Ruppert** et al. 2011			**Our method**	
Dataset	Mean	SD	*P*-value	Mean	SD	*P*-value	Mean	SD	*P*-value	Mean	SD
1	1.480	0.398	0.0046	1.346	0.312	0.0093	1.089	0.281	0.0115	0.703	0.259
2	1.477	0.387	0.0042	1.329	0.310	0.0092	1.096	0.279	0.0117	0.692	0.252
3	1.502	0.401	0.0039	1.358	0.319	0.0095	1.103	0.287	0.0113	0.715	0.264
5	1.469	0.391	0.0040	1.320	0.299	0.0096	1.078	0.268	0.0121	0.679	0.245

Each *P*-value is obtained using mixed model analysis to compare our method with the indicated state-of-the-art method.

methods on each in vivo dataset is shown in Table V. From the statistics results, we can observe that our method also outperforms the other three methods with over two orders of magnitude acceleration. Due to the GPU implementation of parallel SIFT matching and voting, our method achieves a real time performance on the in vivo brain datasets.

IV. DISCUSSION AND CONCLUSION

In this article, we present a novel symmetry axis extraction method from brain images based on parallel SIFT matching and voting. To the best of our knowledge, although SIFT features have been well-validated and heavily used in computer vision, our method is the first attempt to use this well-known feature to detect symmetry axis from the brain image. The stable and real-time performance has been demonstrated by the experiments on both synthetic and real datasets.

Compared with the existing methods for symmetry axis detection from brain images, our method has following advantages: (1) relying on the distinctive SIFT features to extract symmetry axis improves its ability in tolerance to image rotation, noise, and asymmetry, while previous methods mainly used gray level, skull shape, or internal edges to detect symmetry axis, which may easily suffer from interference due to intensity variation, noise or asymmetry; (2) integrating the scale, orientation, and flipped descriptor into a novel metric provides an intuitive and effective way to measure the symmetric similarity for each pair of SIFT features, especially where SIFT descriptor is proved to be invariant to scaling, orientation, affine distortion and intensity changes; (3) clustering and indexing all detected SIFT features using mean-shift and GPU KD-tree enable us to solve the dominant symmetry axis via parallel matching and voting; (4) implementing our method in GPU from SIFT detection to the final parallel matching and voting provides a fully parallel solution for symmetry axis detection from brain images that achieves real-time performance. Experiments on both synthetic and in vivo datasets have demonstrated the above advantages of our method in term of both accuracy and running time comparisons.

Table V. Average running time of different methods for each slice in the vivo in dataset. 55×15mm (300 × 300 DPI)

	Average Running Time (s)				
Dataset	**Hu** et al. 2003	**Song** et al. 2007	**Rupper** et al. 2011	**Our Method (without GPU)**	**Our Method (with GPU)**
1	8.484	4.389	5.935	2.186	0.025
2	8.521	4.327	5.876	2.198	0.026
3	8.466	4.635	5.893	2.203	0.025
4	8.513	4.422	5.964	2.219	0.024
5	8.492	4.296	5.765	2.216	0.025

On the other hand, our method has the following limitations. Similar to the previous methods in detecting symmetry axis from a brain image, our method is also under the assumption that ideal symmetry axis in the brain image is a straight line. Such an assumption may violate with the true anatomical structure of human brain, where the fissure line may sometimes be a curved line even for a normal person. Since there are several situations that only require finding the reference symmetry axis in the brain image, so our method still provides an excellent tool for clinical applications.

In conclusion, we present a fast and robust symmetry axis detection method for brain images. We demonstrated that symmetry axis extraction from brain images can be more accurate and more efficient by parallel matching and voting the distinctive SIFT features, which are detected, clustered, and indexed under a novel parallel framework. Our proposed method is validated on both synthetic and in vivo datasets, including both normal and pathological cases. Convincing experiment results and comparisons have demonstrated the effectiveness of the proposed method. Our future work includes extending our method to extract 3D symmetry plane or perform curve symmetry axis/surface detection for brain images.

ACKNOWLEDGMENTS

This work was supported in part by grants from National Natural Science Foundation of China (No. 61303101, 61170326, 61170077), the Natural Science Foundation of Guangdong Province, China

(No.S2012040008028), the Shenzhen Research Foundation for Basic Research, China (No. JCYJ20120613170718514,No.JCYJ20130326112201234), and the New Teacher Research Funding of Shenzhen University (No. 2012-801).

REFERENCES

B.A. Ardekani, J. Kershaw, M. Braun, and I. Kanno, Automatic detection of mid-sagittal plane in 3D brain images, IEEE Trans Med Imaging 16 (1997), 947–952.

F.P.G. Bergo, A.X. Falcão, C.L. Yasuda, and F. Cendes, FCD segmentation using texture asymmetry of MR-T1 images of the brain, The Fifth IEEE International Symposium on Biomedical Imaging: From Nano to Macro (ISBI), Paris, France, 2008a, pp. 424–427.

F.P.G. Bergo, G.C.S. Ruppert, and A.X. Falcão, Fast and robust mid-sagittal plane location in 3D MR images of the brain, Proceedings of the International Conference on Bioinspired Systems and Signal Processing, 2008b, pp. 92–99.

M.E. Brummer, Hough transform detection of the longitudinal fissure in tomographic head images, IEEE Trans Med Imaging 10 (1991), 74–81.

D. Comaniciu and P. Meer, Mean shift: A robust approach toward feature space analysis, IEEE Trans Pattern Anal 24 (2002), 603–619.

M. Corti, H. Metta, M.F. Villafañe, C. Yampolsky, R. Schtirbu, G. Sevlever, and D. Garrido, Stereotactic brain biopsy in the diagnosis of focal brain lesions in AIDS, Medicina 68 (2008), 285–290.

G. Costantini and D. Casali, Detection of symmetry axis by a CNN-based algorithm, Agios Nikolaos, Crete Island, Greece, 2007, pp. 46–49.

T.J. Cullen, M.A. Walker, S.L. Eastwood, M.M. Esiri, P.J. Harrison, and T.J. Crow, Anomalies of asymmetry of pyramidal cell density and structure in dorsolateral prefrontal cortex in schizophrenia. Br J Psychiatry 188 (2006), 26–31.

E.E. Gilles, M.L. McGregor, and G. Levy-Clarke, Retinal hemorrhage asymmetry in inflicted head injury: A clue to pathogenesis? J Pediatr 143 (2003), 494–499.

G. Gong, T. Jiang, C. Zhu, Y. Zang, F. Wang, S. Xie, J. Xiao, and X. Guo, Asymmetry analysis of cingulum based on scale-invariant parameterization by diffusion tensor imaging, Hum Brain Mapp 24 (2005), 92–98.

D. Grigaitis and M. Meilunas, Automatic extraction of symmetry plane from Falx Cerebri areas in CT slices, Proceeding of Bildverarbeitung fürdie Medizin 2007, Algorithmen, Systeme, Anwendungen, Proceedings des Workshops vom 25–27. März 2007 in München, 2007, pp. 267–271.

M.R. Herbert, D.A. Ziegler, C.K. Deutsch, L.M. O'Brien, D.N. Kennedy, P.A. Filipek, A.I. Bakardjiev, J. Hodgson, M. Takeoka, N. Makris, and V.J. Caviness, Brain asymmetries in autism and developmental language disorder: A nested whole-brain analysis, Brain 128 (2005), 213–226.

G. Hermes, J.W. Ajioka, K.A. Kelly, E. Mui, F. Roberts, K. Kasza, T. Mayr, M.J. Kirisits, R. Wollmann, D.J. Ferguson, C.W. Roberts, J.H. Hwang, T. Trendler, R.P. Kennan, Y. Suzuki, C. Reardon, W.F. Hickey, L. Chen, and R. McLeod, Neurological and behavioral abnormalities, ventricular dilatation, altered cellular functions, inflammation, and neuronal injury in brains of mice due to common, persistent, parasitic infection, J Neuroinflammation 5 (2008), 1–37.

Q. Hu and W.L. Nowinski, A rapid algorithm for robust and automatic extraction of the midsagittal plane of the human cerebrum from neuroimages based on local symmetry and outlier removal, NeuroImage 20 (2003), 2153–2165.

S. Joshi, P. Lorenzen, G. Gerig, and E. Bullitt, Structural and radiometric asymmetry in brain images, Med Image Anal 7 (2003), 155–170.

A. Kumar, E.A. Schmidt, M. Hiler, P. Smielewski, J.D. Pickard, and M. Czosnyka, Asymmetry of critical closing pressure following head injury, J Neurol Neurosurg Psychiatry 76 (2005), 1570–1573.

S.X. Liu, Symmetry and asymmetry analysis and its implications to computer-aided diagnosis: A review of the literature, J Biomed Inform 42 (2009), 1056–1064.

S.X. Liu, C. Imielinska, A. Laine, W.S. Millar, E.S. Connolly, and A.L. D'Ambrosio, Asymmetry analysis in rodent cerebral ischemia models, Acad Radiol 15 (2008), 1181–1197.

S.X. Liu, J. Kender, C. Imielinska, and A. Laine, Employing symmetry features for automatic misalignment correction in neuroimages, J Neuroimaging 21 (2011), 15–33.

Y. Liu, R.T. Collins, and W.E. Rothfus, Robust midsagittal plane extraction from normal and pathological 3-D neuroradiology image, IEEE Trans Med Imaging 20 (2001), 173–192.

Y. Liu, L.A. Teverovskiy, O.L. Lopez, H. Aizenstein, C.C. Meltzer, and J.T. Becker, Discovery of biomarkers for Alzheimer's disease prediction from structural MR images, Arlington, VA, USA 2007, pp. 1344–1347.

P. Lorenzen, S. Joshi, G. Gerig, and E. Bullitt, Tumor-induced structural and radiometric asymmetry in brain images, Kauai, Hawaii, USA, 2001, pp. 163–170.

D. Lowe, Distinctive image features from scale-invariant keypoints. Int J Comput Vis 60 (2004), 91–110.

V. Oertel-Knöchel and D.E. Linden, Cerebral asymmetry in schizophrenia, Neuroscientist, 17 (2011), 456–467.

S. Prima and N.W. Daesslé, Computation of the mid-sagittal plane in diffusion tensor MR brain images, Proceedings of SPIE: Medical Imaging 6512 (2007), 1–9.

S. Prima, S. Ourselin, and N. Ayache, Computation of the midsagittal plane in 3D brain images, IEEE Trans Med Imaging 21 (2002), 122–138.

D. Reisfeld, H. Wolfson, and Y. Yeshurun, Context free attentional operators: The generalized symmetry transform, Int J Comp Vis 14 (1995), 119–130.

M. Roussigne, P. Blader, and S.W. Wilson, Breaking symmetry: The zebrafish as a model for understanding left-right asymmetry in the developing brain, Dev Neurobiol 72 (2012), 269–281.

S. Roy and S.K. Bandyopadhyay, Detection and quantification of brain tumor from MRI of brain and it's symmetric analysis, Int J Inform Commun Technol Res 2 (2012), 477–483.

G.C.S. Ruppert, L.A. Teverovskiy, C.P. Yu, A.X. Falcão, and Y. Liu, A new symmetry-based method for mid-sagittal plane extraction in neuroimages, Chicago, IIIinois, USA, 2011, pp. 285–288.

V.M. Saenger, F.A. Barrios, M.L. Martinez-Gudino, and S. Alcauter, Hemispheric asymmetries of functional connectivity and grey matter volume in the default mode network, Neuropsychologia 50 (2012), 1308–1315.

E. Song, Q. Wang, G. Ma, and H. Liu, Symmetry analysis to detect pathological brain in MRI, Wuhan, China, 6789 (2007), 1–6.

M. Stegmann, K. Skoglund, and C. Ryberg, Mid-sagittal plane and midsagittal surface optimization in brain MRI using a local symmetry measure, San Diego, CA, USA, 2005, pp. 568–579.

H. Takao, O. Abe, H. Yamasue, S. Aoki, K. Kasai, and K. Ohtomo, Cerebral asymmetry in patients with schizophrenia: A voxel-based morphometry (VBM) and diffusion tensor imaging (DTI) study, J Magn Reson Imaging 31 (2010), 221–226.

L.A. Teverovskiy, J. Becker, O. Lopez, and Y. Liu, Quantified brain asymmetry for age estimation of normal and Alzheimer's disease/mild cognitive impairment subjects, Paris, France: From Nano to Macro (ISBI), 2008, pp. 1509–1512.

L.A. Teverovskiy and Y. Liu, Truly 3D midsagittal plane extraction for robust neuroimage registration, Arlington, Virginia, 2006, pp. 860–863.

S. Tilman, M.M. Eva, R. Torsten, P. Adolf, and V.S. Edith, White matter fiber degradation attenuates hemispheric asymmetry when integrating visuomotor information, J Neurosci 30 (2010), 12168–12178.

L. Tommasi, Mechanisms and functions of brain and behavioural asymmetries, Philos Trans Roy Soc Lond B Biol Sci 364 (2009), 855–859.

A. Tuzikov, O. Colliot, and I. Bloch, Evaluation of the symmetry plane in 3D MR brain images, Pattern Recogn Lett 24 (2003), 2219–2233.

I. Volkau, K.N.B. Prakash, A. Ananthasubramaniam, A. Aziz, and W. L. Nowinski, Extraction of the midsagittal plane from morphological neuroimages using the Kullback-Leibler's measure, Med Image Anal 10 (2006), 863–874.

C.P. Yu, G.C.S. Ruppert, D.T.D. Nguyen, A.X. Falcão, and Y. Liu, Statistical asymmetry-based brain tumor segmentation from 3D MR images, Vilamoura, Algarve, Portugal (BIOSIGNALS), 2012, pp. 527–533.

Y. Zhang, and Q. Hu, A PCA-based approach to the representation and recognition of MR brain midsagittal plane images, Vancouver, Canada, 2008, pp. 3916–3919.

W.L. Zhao, and C.W. Ngo, Flip-invariant SIFT for copy and object detection, IEEE Trans Image Process 22 (2013), 980–991.

F. Zhou, Y. Zhao, and K.L. Ma, Parallel mean shift for interactive volume segmentation, Machine Learning in Medical Imaging (Lecture Notes in Computer Science), 6357, 2010, pp. 67–75.

K. Zhou, Q.M. Hou, R. Wang, and B.N. Guo, Real-time KD-tree construction on graphics hardware, ACM Trans Graphics 27 (2008), 126.